Hindawi
International Transactions on Electrical Energy Systems
Volume 2024, Article ID 6690355, 14 pages
https://doi.org/10.1155/2024/6690355

Research Article

A Control Architecture for Regulating Voltage and Power Flows in a Networked Microgrid System

Thomas John and Umar Khan

Computer Science Department, Edge Hill University, Ormskirk L39 4QP, UK

Correspondence should be addressed to Thomas John; thomas.john@edgehill.ac.uk

Received 2 June 2023; Revised 11 January 2024; Accepted 20 January 2024; Published 1 February 2024

Academic Editor: Faroque Azam

This paper presents a unique control system to regulate power exchanges and load bus voltage in a networked microgrid (NMG) system comprising AC and DC microgrids. During the islanding of a microgrid in this NMG system, load voltage and power balance can get disturbed. A control system and associated converter and inverter control methods are presented to rectify these issues. An efficient model predictive control (MPC) method, which gives a tracking error of 50% lower than a conventional proportional-integral (PI) controller, is used to control multiple inverters in the NMG system. Simulation studies are conducted to test the NMG in islanding and load change scenarios. With the help of these studies, it is verified that the MPC-controlled inverters can provide better tracking accuracy in achieving desired power flows in the NMG system.

1. Introduction

There has been growing interest in studying the power flows among a network of interconnected microgrids [1, 2]. These interconnected microgrids can be called networked microgrid (NMG) or multi-microgrid (MMG) systems. Real-world applications of networked microgrids are given in detail in [3]. Several research works have been carried out on laboratory-based small-scale multi-microgrid systems, such as in [4, 5]. An interconnected microgrid system is developed in [4], where two AC microgrids are interconnected through a separate switch. This NMG system in [4] can operate separately as individual microgrids when the switch is opened and as a single microgrid if the switch is closed. In [5], another NMG test system, consisting of three AC microgrids connected to a common central AC bus, is presented. In this NMG system, microgrids can operate in independent and interconnected modes. Other types of microgrid clusters such as interlinked AC microgrid clusters [6], DC microgrid clusters [7], and hybrid AC/DC microgrid clusters [8–11] are also proposed. From the control perspective, most of these papers emphasize the control methodologies of the interconnecting converters installed between these microgrids rather than the operating modes of these interconnected microgrids and the power exchange between these microgrids. Moreover, in all these papers, the networked microgrid or multi-microgrid system contains closely spaced microgrids or microgrids connected to adjacent feeders, forming single area power systems. As a result, adequate research essentially needs to be undertaken on networked multi-area microgrids containing AC and DC microgrids, which are separated by large distances and interlinked by longer tie lines.

Several challenges exist in operating interconnected or intertied microgrids, such as power quality issues, power flow control, and islanded conditions. In an NMG system, a given microgrid can operate in different modes, such as grid-connected, islanded, and interconnected modes. In grid-connected mode, a given microgrid in an NMG system is connected to the grid, whereas other microgrids in the NMG system may or may not be grid-connected or islanded. In islanded mode, a given microgrid in an NMG system is disconnected from the grid, but other microgrids in the NMG system may or may not be islanded or grid-connected. In interconnected mode, a given microgrid in an NMG system is connected to another microgrid but other

microgrids may be interconnected, grid-connected, or islanded. Therefore, many operation modes and scenarios can exist for a given microgrid in an NMG system. Given these numerous operational challenges, an efficient control and coordination strategy is necessary for a networked or multi-microgrid system to provide the desired load voltage and power under several operation modes and scenarios.

The existing literature presents various control strategies to control the converter-interfaced distributed generations (DGs) in microgrids and networked microgrids [12]. Various conventional voltage and current control methods, such as droop control, are available to control the converters in microgrid systems [13, 14]. But in case of droop control, power sharing is affected by variations in tie-line impedances in NMG systems [15, 16]. The solution to this problem is to propose a generalized control architecture comprising a distinctive local converter control technique called model predictive control (MPC), a popular control technique for converters. MPC's primary idea is to use a system model to predict the future behaviour of the controlled variables [17]. Compared with conventional control techniques such as droop and proportional-integral (PI) controls, the significant benefits of the proposed MPC are that it does not require the need of modulators, coordinate transformations, and voltage and current loops [17]. There are two MPC methods: finite control set MPC and continuous set MPC. The continuous set MPC needs an additional modulator to generate the switching signals. So, a finite control set MPC is preferred to control converters in the proposed NMG system. In [17], a finite control set MPC scheme, which controls different converters, is presented. In [18], MPC is used to control parallel-connected inverters. Unlike the previously used MPC methods, the proposed MPC algorithm is independent of the line and load impedances of the given NMG system, thereby ensuring a small steady-state error and faster dynamic response under different operating scenarios.

Several MPC-based control architectures for microgrid systems are proposed in [19–21]. In comparison with these works, the novelty of the proposed paper is that a unique control architecture is developed for a ring-shaped NMG system. This architecture comprises MPC-based primary controllers and a centralized tertiary controller, thereby eliminating the need for a secondary controller. Thus, the control architecture of the NMG system gets simplified, the cost of implementing such an architecture gets reduced, and the scalability of such an architecture will be improved, especially when there are several interconnected microgrids in the NMG system.

The essential features to be highlighted in this paper are as follows: (1) a distinct architecture has been proposed for a networked ring-shaped microgrid system consisting of AC and DC microgrids, (2) an advanced MPC method is used for controlling multiple converters in the networked microgrid system, and (3) problems such as power imbalance and DC voltage variation are solved during various operating conditions of a DC microgrid such as islanding and load changes in the given networked microgrid system.

The contents presented in this paper are available in Chapter 4 in the doctoral thesis written and published by the first author [22].

2. Description of the NMG System

A ring-shaped architecture is proposed for an NMG system, shown in Figure 1. This system consists of three microgrids, each separated by about 10 km. Microgrid 2 is a DC microgrid. Microgrids 1 and 3 are AC microgrids. AC microgrids are interconnected through line 3. The DC microgrid is connected to the AC microgrids through interconnecting inverters 1 and 2 and lines 1 and 2. Every microgrid is interconnected to its corresponding distribution grid through a 0.4/22 kV distribution transformer. $V_{L1}\angle\delta_1$, V_{L2}, and $V_{L3}\angle\delta_3$ are the voltages at the load buses in the given microgrids. The output voltages of the interconnecting inverters are denoted by $V_{n1}\angle\delta_{n1}$ and $V_{n2}\angle\delta_{n2}$. $V_i\angle\delta_i$ ($i = 1$, 2, and 3) is the voltage at the end of each line. R_{ti} ($i = 1$, 2, and 3) and L_{ti} ($i = 1$, 2, and 3) are the resistance and inductance of the lines. The real and reactive power flows at the sending ends of the lines are denoted by P_{si} ($i = 1$, 2, and 3) and Q_{si} ($i = 1$, 2, and 3). The real and reactive powers at the receiving ends of the lines are denoted by P_{ri} ($i = 1$, 2, and 3) and Q_{ri} ($i = 1$, 2, and 3).

Figure 2 shows the system configuration of an AC microgrid used in the proposed NMG system. The AC microgrid consists of a DG unit, a storage battery unit, and an AC load. Different interfacing inverters are used to connect the DG and storage battery units to the AC load bus. P_{di} ($i = 1$, 2, and 3) and Q_{di} ($i = 1$, 2, and 3) are the real and reactive power outputs of DG inverters. P_{bi} ($i = 1$, 2, and 3) and Q_{bi} ($i = 1$, 2, and 3) are real and reactive power outputs of battery inverters.

The schematic block diagram of the DC microgrid used in the proposed NMG system is shown in Figure 3. The DC microgrid consists of a DG unit, a storage battery unit, and a supercapacitor unit. The DG, storage battery, and supercapacitor units are connected to the DC load bus through their DC/DC buck converters 2a, 2b, and 2c. P_{d2}, P_{b2}, and P_{s2} are the real power outputs of converters 2a, 2b, and 2c, respectively. There are generally two modes of operation of the converters and inverters in the proposed NMG system. One mode is called current control mode (CCM), where the output current of the inverter or converter is controlled at the desired value. The other mode is the voltage control mode (VCM), where the output voltage of the inverter or converter is regulated at the required value.

There are two modes of operation of the NMG system: (1) grid-connected mode in which all microgrids are connected to their respective distribution grids; and (2) islanded mode in which 1 microgrid or more than one microgrid gets disconnected from their corresponding distribution grid.

When an AC microgrid is grid-connected, the grid controls the load bus voltage, and all inverters within the AC microgrid operate in CCM. During the islanding of AC microgrid, the battery inverter in the AC microgrid goes into VCM mode and the other inverter continues to operate in CCM mode.

During the grid-connected mode of the DC microgrid, the AC/DC converter connected to distribution grid 2 controls the DC load bus voltage and all the different converters within the DC microgrid operate in CCM. When

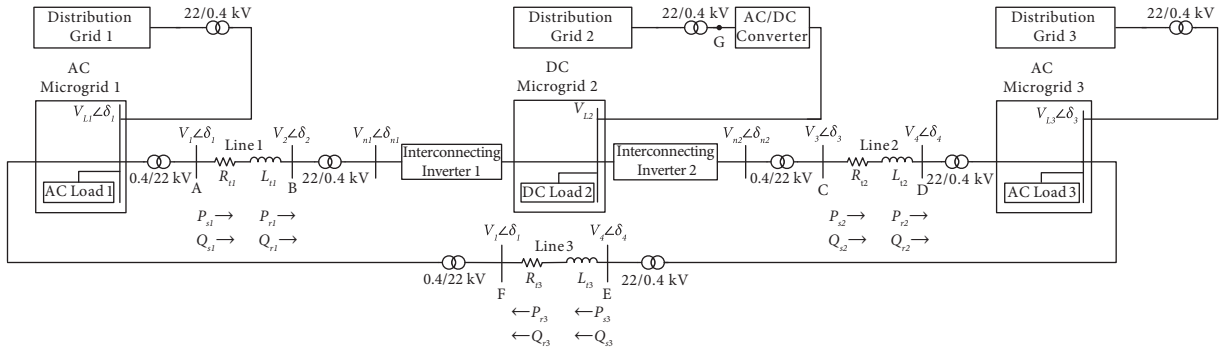

Figure 1: Proposed ring-shaped architecture of a NMG system.

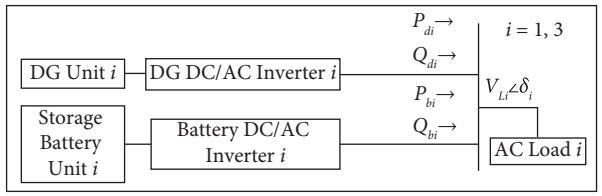

Figure 2: System configuration of AC microgrids 1 and 3.

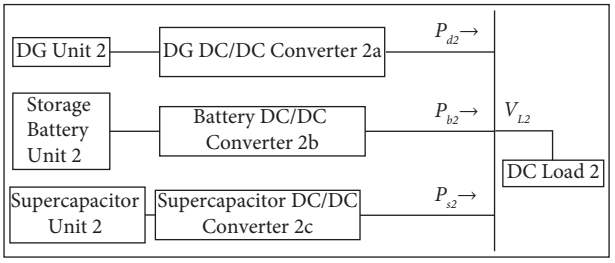

Figure 3: Schematic block diagram of DC microgrid 2.

the DC microgrid is islanded, the battery converter in the DC microgrid goes into VCM mode, and the other converters continue in CCM mode.

The concept of power exchange between the microgrids in this NMG system is fundamentally related to the control of real and reactive power flows based on the power flow equations [23]. If line voltages $V_1 = V_2 = V_3 = V$, considering both the resistances and reactances of the lines, real and reactive powers at the sending and receiving ends of the interconnecting lines are given below:

$$P_{si} = \left(\frac{V^2}{Z_{ti}}\right)\cos\theta_{ti} - \left(\frac{V^2}{Z_{ti}}\right)\cos\left(\theta_{ti} + \delta_{i,i+1}\right) \quad \text{for } i = 1,\ 2 = \left(\frac{V^2}{Z_{ti}}\right)\cos\theta_{ti} - \left(\frac{V^2}{Z_{ti}}\right)\cos\left(\theta_{ti} + \delta_{i,1}\right) \quad \text{for } i = 3, \tag{1}$$

$$\mathrm{P_{ri}} = \left(\frac{\mathrm{V}^2}{\mathrm{Z_{ti}}}\right)\cos\left(\theta_{\mathrm{ti}} - \delta_{\mathrm{i,i+1}}\right) - \left(\frac{\mathrm{V}^2}{\mathrm{Z_{ti}}}\right)\cos\theta_{\mathrm{ti}} \quad \text{for i} = 1,\ 2 = \left(\frac{\mathrm{V}^2}{\mathrm{Z_{ti}}}\right)\cos\left(\theta_{\mathrm{ti}} - \delta_{\mathrm{i,1}}\right) - \left(\frac{\mathrm{V}^2}{\mathrm{Z_{ti}}}\right)\cos\theta_{\mathrm{ti}} \quad \text{for i} = 3, \tag{2}$$

$$\begin{aligned} \mathrm{Q_{si}} &= \left(\frac{\mathrm{V}^2}{\mathrm{Z_{ti}}}\right)\sin\theta_{\mathrm{ti}} - \left(\frac{\mathrm{V}^2}{\mathrm{Z_{ti}}}\right)\sin\left(\theta_{\mathrm{ti}} + \delta_{\mathrm{i,i+1}}\right) \quad \text{for i} = 1,\ 2 = \left(\frac{\mathrm{V}^2}{\mathrm{Z_{ti}}}\right)\sin\theta_{\mathrm{ti}} - \left(\frac{\mathrm{V}^2}{\mathrm{Z_{ti}}}\right)\sin\left(\theta_{\mathrm{ti}} + \delta_{\mathrm{i,1}}\right) \quad \text{for i} = 3, \\ \mathrm{Q_{ri}} &= \left(\frac{\mathrm{V}^2}{\mathrm{Z_{ti}}}\right)\sin\left(\theta_{\mathrm{ti}} - \delta_{\mathrm{i,i+1}}\right) - \left(\frac{\mathrm{V}^2}{\mathrm{Z_{ti}}}\right)\sin\theta_{\mathrm{ti}} \quad \text{for i} = 1,\ 2 = \left(\frac{\mathrm{V}^2}{\mathrm{Z_{ti}}}\right)\sin\left(\theta_{\mathrm{ti}} - \delta_{\mathrm{i,1}}\right) - \left(\frac{\mathrm{V}^2}{\mathrm{Z_{ti}}}\right)\sin\theta_{\mathrm{ti}} \quad \text{for i} = 3, \end{aligned} \tag{3}$$

where $\delta_{i,i+1} = \delta_i - \delta_{i+1}$ (for $i = 1, 2$) = phase angle difference between voltages V_i and V_{i+1}; $\delta_{i,1} = \delta_i - \delta_1$ (for $i = 3$) = phase angle difference between voltages V_i and V_1; δ_i = phase angle of voltage V_i for $i = 1$, 2, and 3; and $Z_{ti}\angle\Theta_{ti}$ = impedance of line i.

Both resistances and reactances of the lines are considered in these equations because NMG is a medium-voltage level distribution system. Generally, in a power or NMG system, the voltage magnitude at the load bus is maintained at nominal values to keep the loads in proper operation [23]. Therefore, to control the real power exchanges in the NMG system, the phase angles of the AC load bus voltages or output AC voltages of the interconnecting inverters need to be varied. Thus, an effective control method, as explained in the following section, needs to be developed to achieve that phase angle variation.

3. Control Method of Converters in the NMG System

MPC has been gaining wide interest in the control of various types of converters in recent years. Also, due to the advancement and development of fast microprocessors and the discrete nature of converters, MPC is gaining popularity in converter control in several microgrid applications [17]. The basic principle of MPC lies in using a system model and a suitable cost function to predict the behaviour of controlled variables in the given system [17]. It has several advantages such as its applicability to both single-input single-output (SISO) and multi-input multi-output (MIMO) systems [17] and easy inclusion of constraints. Moreover, unlike other conventional control methods, such as proportional-integral (PI) and hysteresis control, MPC does not need modulators, cascade control loops, and coordinate transformations [17].

In this paper, an advanced MPC method is developed to control two main types of converters, namely, DC/DC and DC/AC converters, in the given NMG system. The benefit of using this advanced MPC method is that it can be applied to multiple converters without any modifications. To control an AC/DC converter in the same NMG system, proportional-integral (PI) and hysteresis controllers but not MPC is used because MPC becomes computationally intensive if applied to all converters. Each converter control technique is discussed in detail as follows.

3.1. AC/DC Converter Model and Control. In Figure 4, the power circuit of an AC/DC converter consisting of 6 transistor switches is shown. This converter is used to convert the AC voltage of distribution grid 2 into DC output voltage, to be fed to DC microgrid. The three-phase supply voltages of distribution grid 2 at the input side of the AC/DC converter are e_{ga}, e_{gb}, and e_{gc}. The three-phase currents supplied by distribution grid 2 are i_{ga}, i_{gb}, and i_{gc}. The proposed control method for the AC/DC converter is shown in Figure 5. This control method regulates the DC output voltage V_{dc1} of AC/DC converter and compensates for any variation V_{dc1} due to any power imbalance in DC microgrid 2.

The power imbalance will induce a voltage error $(V^*_{\mathrm{dc1}} - V_{\mathrm{dc1}})$, which is then fed into a PI controller to generate a current reference i^*_d and thereby to track i_d. To eliminate the presence of high-frequency switching ripples at the distribution grid side, V_{dc1} is first passed through a first-order low-pass filter (LPF). i_d is the real component of the grid current and i_q is the reactive component of the grid current. The current i_q is maintained at 0 A, so distribution grid 2 delivers only real and no reactive power. The current errors Δi_d and Δi_q are then converted from dq reference frame into abc reference frame and fed into a hysteresis controller and a pulse width modulator (PWM) to generate the required control signals. The measured grid currents of each phase need to be compared with the corresponding references using the hysteresis controller. This is the reason why we need to use dq to abc conversion as shown in Figure 5. Thus, as shown in Figure 5, by efficiently controlling the AC input current or power inputs of the AC/DC converter, the output DC voltage of this converter can be maintained at the rated nominal value.

3.2. DC/DC Converter Model and Control. Figure 6 shows the single-phase DC/DC buck converter model used in the DC microgrid in the NMG system. A buck converter steps down or decreases the DC input voltage, and the input DC voltage and diode voltage of the DC/DC buck converters are represented by v_{in} and v_i, respectively. MPC is used to control the DC/DC converter. So, a converter model needs to be developed.

When Kirchhoff's voltage and current laws are applied to the converter model, the following equations are obtained:

$$L_m\left(\frac{di_l}{dt}\right) = v_i - v_m, \tag{4}$$

$$C_m\left(\frac{\mathrm{d}v_m}{dt}\right) = i_l - i_m, \tag{5}$$

where i_l is the current which flows through inductor L_m, i_m is the output current, and v_m is the output voltage across capacitor C_m. Due to high sampling frequency, the following assumption can be made:

$$\frac{di_m}{dt} = 0. \tag{6}$$

The relationship between v_{in} and v_i can be expressed as

$$\begin{aligned} v_i &= Sv_{in} \\ &= u_1, \end{aligned} \tag{7}$$

where u_1 is the control input and S is the state of the switch which can be defined as follows:

$$S = \begin{cases} 1, & \text{switch is ON,} \\ 0, & \text{switch is OFF.} \end{cases} \tag{8}$$

On substituting (7) into (4) and on further simplification of (4)–(6), the discrete state-space model of the DC/DC converter system is derived as follows:

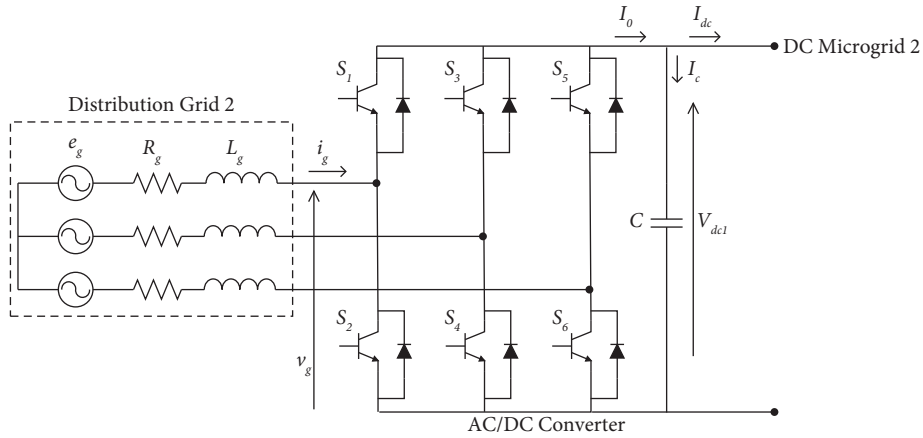

Figure 4: Power circuit of AC/DC converter, which is connected to distribution grid 2.

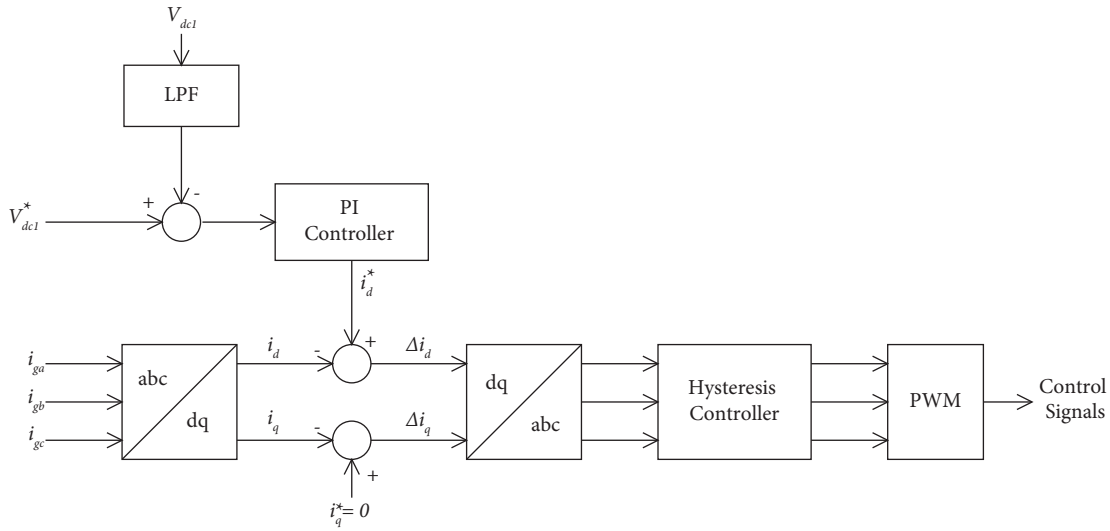

Figure 5: Control method for AC/DC converter.

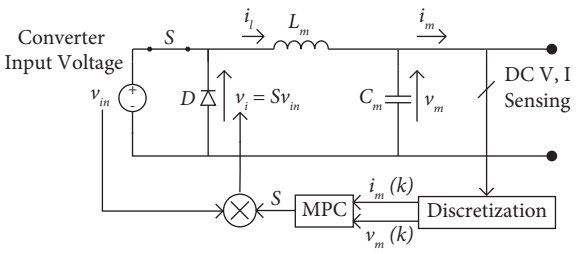

Figure 6: DC/DC buck converter model.

$$x_1(k+1) = A_d x_1(k) + B_d u_1(k),$$
$$y_1(k) = C_d x_1(k), \tag{9}$$

where $x_1(k) = \left[\, i_l(k) \;\; v_m(k) \;\; i_m(k) \,\right]^T$ is the state vector, $u_1(k)$ is the control input vector, $y_1(k)$ is the output vector, T_s is sampling time, and A_d, B_d, and C_d are discretized coefficients as follows:

$$A_d = \begin{bmatrix} 1 & \dfrac{-T_s}{L_m} & 0 \\ \dfrac{T_s}{C_m} & 1 & \dfrac{-T_s}{C_m} \\ 0 & 0 & 1 \end{bmatrix},$$
$$B_d = \begin{bmatrix} \dfrac{T_s}{L_m} & 0 & 0 \end{bmatrix}^T, \tag{10}$$
$$C_d = \begin{cases} \left[\, 0 \;\; 0 \;\; 1 \,\right] \text{in CCM}, \\ \left[\, 0 \;\; 1 \;\; 0 \,\right] \text{in VCM}. \end{cases}$$

From the discrete state-space model, the augmented state-space model of the converter is obtained as follows:

$$X_e(k+1) = A_e X_e(k) + B_e U_e(k), \tag{11}$$

$$Y_e(k) = C_e X_e(k), \tag{12}$$

where $X_e(k) = [\,\Delta i_l(k)\ \ \Delta v_m(k)\ \ \Delta i_m(k)\ \ i_m(k)\,]^T$ is the state vector, $U_e(k) = \Delta u_1(k)$ is the control input vector, and $Y_e(k)$ is the output vector, which is either converter output current or voltage.

$$A_e = \begin{bmatrix} 1 & \dfrac{-T_s}{L_m} & 0 & 0 \\ \dfrac{T_s}{C_m} & 1 & -\dfrac{T_s}{C_m} & 0 \\ 0 & 0 & 1 & 0 \\ 0 & 0 & 1 & 1 \end{bmatrix},$$

$$C_e = \begin{bmatrix} 0 \\ 0 \\ 0 \\ 1 \end{bmatrix}^T, \tag{13}$$

$$B_e = \begin{bmatrix} \dfrac{T_s}{L_m} \\ 0 \\ 0 \\ 0 \end{bmatrix}.$$

Thus, depending upon the value of the output vector, we can control the output voltage or current of a DC/DC converter using MPC. The methods of deriving the discrete state-space model from the continuous state-space model and the augmented state-space model from the discrete-state space model are given in [24].

3.3. DC/AC Converter (Inverter) Model and Control. Figure 7 shows the generalized model of DG, battery, and interconnecting inverters used in the AC microgrid in the NMG system.

The discrete state-space model of the inverter is first derived and then converted into an augmented state-space model, as done with the converter in the previous section. Using Kirchhoff's voltage and current laws, the following equations are obtained from Figure 7.

$$u_2 V_{\mathrm{dc2}} = i_d R + L_f\left(\frac{di_d}{dt}\right) + v_0, \tag{14}$$

$$i_d = C_f\left(\frac{\mathrm{d}v_0}{dt}\right) + i_0, \tag{15}$$

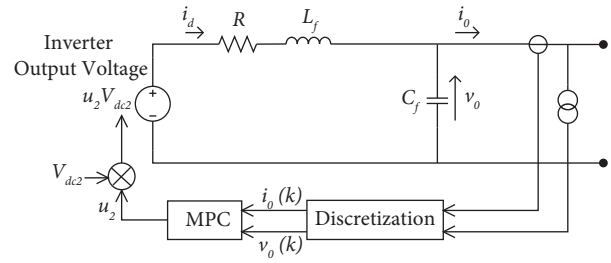

Figure 7: Single-phase inverter model.

where the internal loss of the inverter is R, inductance and capacitance of the LC filter are L_f and C_f, respectively, the current flow through L_f is i_d, the output current is i_0, control input is u_2, the input voltage is V_{dc2}, and the output voltage is v_0. Because of the high sampling frequency, the following assumption is made:

$$\left(\frac{di_0}{dt}\right) = 0. \tag{16}$$

From (14) and (15), the discrete state-space model for MPC is obtained as follows:

$$\begin{aligned} x_2(k+1) &= A_g x_2(k) + B_g u_2(k), \\ y_2(k) &= C_g x_2(k), \end{aligned} \tag{17}$$

where $x_2(k) = [\,i_d(k)\ \ v_0(k)\ \ i_0(k)\,]^T$ is the state vector, $u_2(k)$ is the control input vector, $y_2(k)$ is the output vector, T_s is the sampling time, and A_g, B_g, and C_g are discretized coefficients as follows:

$$A_g = \begin{bmatrix} 1 - \dfrac{\mathrm{R}T_s}{L_f} & \dfrac{-T_s}{L_f} & 0 \\ \dfrac{T_s}{C_f} & 1 & \dfrac{-T_s}{C_f} \\ 0 & 0 & 1 \end{bmatrix}, \tag{18}$$

$$B_g = \begin{bmatrix} \dfrac{V_{dc2}T_s}{L_f} & 0 & 0 \end{bmatrix}^T,$$

$$C_g = \begin{cases} [\,0\ \ 0\ \ 1\,] \text{ in CCM}, \\ [\,0\ \ 1\ \ 0\,] \text{ in VCM}. \end{cases}$$

Using the discrete state-space model, the augmented state-space model of the inverter is obtained as follows:

$$X_h(k+1) = A_h X_h(k) + B_h U_h(k), \tag{19}$$

$$Y_h(k) = C_h X_h(k), \tag{20}$$

where $X_h(k)$ is the state vector.

$$X_h(k) = [\,\Delta i_d(k)\ \ \Delta v_0(k)\ \ \Delta i_0(k)\ \ i_0(k)\,]^T, \tag{21}$$

where $U_h(\mathrm{k}) = \Delta u_2(k)$ is the control input vector and $Y_h(k)$ is the output vector, which is either the inverter output current or voltage.

$$A_h = \begin{bmatrix} 1 - \left(\frac{\mathrm{RT}_s}{L_f}\right) & \frac{-T_s}{L_f} & 0 & 0 \\ \frac{T_s}{C_f} & 1 & -\frac{T_s}{C_f} & 0 \\ 0 & 0 & 1 & 0 \\ 0 & 0 & 1 & 1 \end{bmatrix}, C_h = \begin{bmatrix} 0 & 0 & 0 & 1 \end{bmatrix}, \quad (22)$$

$$B_h = \begin{bmatrix} \frac{V_{dc2}T_s}{L_f} & 0 & 0 & 0 \end{bmatrix}^T.$$

To control the augmented state-space models of the converter and inverter in (11) and (19), respectively, quadratic programming is used to minimize the following objective function [24]:

$$J = (R_s - Y)^T (R_s - Y), \quad (23)$$

subject to the input and input increment constraints as follows:

$$\begin{aligned} 1 \le \mathrm{u}_1(k) \le -1; -1 \le \Delta \mathrm{u}_1(k) \le 1; \\ -1 \le \mathrm{u}_2(k) \le 1; -1 \le \Delta \mathrm{u}_2(k) \le 1, \end{aligned} \quad (24)$$

where R_s is the set-point matrix and Y is the output matrix of the augmented model, which is either Y_e in (12) or Y_h in (20).

Therefore, based on the value of the output matrix, we can control an inverter's output voltage or current using MPC.

4. Control Architecture of the NMG System

As shown in Figure 8, control architecture is proposed for the NMG system. It follows a hierarchy of control levels, containing a centralized controller for the entire NMG system and individual local controllers (LCs) for each of the different converters and inverters in the NMG system. The main objective of the centralized controller is to obtain system information on the NMG system such as load bus voltages, load demands, and operation modes of the microgrids. Based on this information, the centralized controller carries out different functions: (1) it sends reference real and reactive power output signals, $P_{\mathrm{di(ref)}}, Q_{\mathrm{di(ref)}}$ ($i = 1, 3$) and $P_{\mathrm{bi(ref)}}, Q_{\mathrm{bi(ref)}}$ ($i = 1, 3$), to the LCs of the DG and battery inverters during grid-connected modes of AC microgrids; (2) it sends reference load bus voltage signals $V_{Li(\mathrm{ref})}\angle\delta_{i(\mathrm{ref})}$ ($i = 1, 3$) to LCs of the battery inverters during islanded modes of AC microgrids; (3) it sends reference real power output signals $P_{d2(\mathrm{ref})}, P_{b2(\mathrm{ref})}$, and $P_{s2(\mathrm{ref})}$ to LCs of respective converters during grid-connected mode of the DC microgrid; (4) it sends reference load bus voltage signal V_{L2} to LC of the battery converter during islanded mode of the DC microgrid; and (5) it sends reference voltage signals $V_{n1(\mathrm{ref})}\angle\delta_{n1(\mathrm{ref})}$ and $V_{n2(\mathrm{ref})}\angle\delta_{n2(\mathrm{ref})}$ to LCs of interconnecting inverters during both grid-connected and islanded modes of the DC microgrid. As explained in the previous section, the different LCs use the advanced MPC method to generate and send the optimal switching signals to the corresponding inverters and converters. Moreover, a high-speed reliable communication network is essential for the efficient operation of the NMG system, to maintain effective coordination among the centralized and local controllers [25].

AC and DC microgrids can operate either in grid-connected or islanded modes. When an AC microgrid is grid-connected, the DG inverter in the microgrid is made to provide a prespecified amount of real and reactive power to the load and the battery inverter acts as the back-up inverter. In the instance of islanding of an AC microgrid, the centralized controller, on detecting a frequency drop in the system, sends the required voltage reference signal to the LC of the battery inverter in the islanded AC microgrid.

When DC microgrid is grid-connected, the DG converter in the microgrid is controlled to deliver a prespecified amount of real power to the load and converters of battery and supercapacitor units serve as back-up converters. In case of the DC microgrid islanding, a voltage drop occurs in the DC microgrid. When the centralized controller detects this voltage drop, it sends the required voltage reference signal to the LC of the battery converter. It sends the voltage reference signal also to the supercapacitor converter's LC to regulate the DC load bus voltage, until the battery in DC microgrid ramps up its power output. During the islanding of the DC microgrid, phase angles of the output voltages of the interconnecting inverters are calculated based on the desired real power to be obtained at the receiving ends of lines adjacent to the interconnecting inverters. This phase angle is determined from (2) as follows:

$$\begin{aligned} \delta_{n1(\mathrm{ref})} &= \delta_{n2(\mathrm{ref})} = \delta_{i,i+1(\mathrm{ref})} \\ &= \theta_{ti} - \cos^{-1}\left[\frac{P_{\mathrm{ri(ref)}}Z_{ti}}{V^2} + \cos\theta_{ti}\right], \quad \text{for } i = 1, 2, \end{aligned} \quad (25)$$

where $\delta_{i,i+1(\mathrm{ref})}$ is the reference phase angle difference between V_i and V_{i+1}, $\delta_{n1(\mathrm{ref})}$ and $\delta_{n2(\mathrm{ref})}$ are the reference phase angles of output voltages of the interconnecting inverters, and $P_{ri(\mathrm{ref})}$ is the reference real power to be maintained at the receiving end of line i. Then, in line i, the corresponding sending end real power flow and sending and receiving end reactive power flows are obtained by substituting the above calculated value of the reference phase angle into (1), (3), and (4). The centralized controller, while monitoring the load bus voltage in the DC microgrid, triggers undervoltage load shedding whenever the DC load bus voltage deviation crosses the tolerance limit of +5% of the nominal value of 380 V. 380 V is the standard DC nominal voltage currently adopted by EMERGE Alliance for use in data centers, telecom systems, etc. [26]. The allowable tolerance limit for the

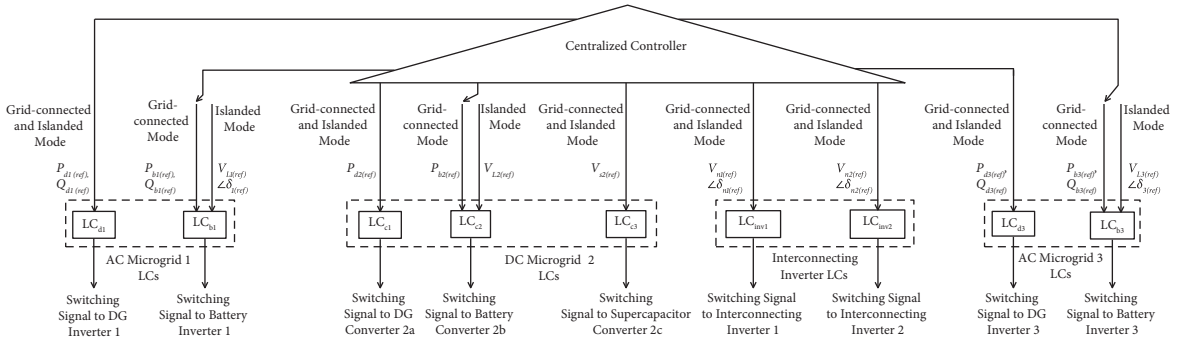

Figure 8: Control architecture for the NMG system.

DC bus voltage is ±5% of 380 V [26]. In the proposed NMG system, an under voltage load shedding (UVLS) scheme, similar to that given in [27], is developed here for the islanded DC microgrid: (1) when the DC load bus voltage drops to 95% of the nominal value, 15% load is shed in the DC microgrid; (2) when the DC load bus voltage drops to 93% of the nominal value, 10% additional load is shed in the DC microgrid; and (3) when the DC load bus voltage drops below 90% of the nominal value, 5% additional load is shed in the DC microgrid. If the DC load bus voltage does not recover after adopting UVLS, then interconnecting lines in the NMG are disconnected and noncritical loads in the DC microgrid are shed.

5. Simulation Studies

The three different microgrids in the proposed NMG systems are capable of grid-connected and islanded modes. To demonstrate the capability and performance of the NMG system, three test cases are simulated using MATLAB/Simulink. In the first test case, DC microgrid 2 is islanded or disconnected from distribution grid 2 to verify whether the DC load bus voltage can be properly regulated or not. Mutual power sharing is an important advantage of using an NMG system. So, in the second test case, under the power deficit condition in DC microgrid 2, the exchange of power between the islanded DC microgrid and adjacent grid-connected AC microgrids is simulated. Finally, in the third test case, during a worst-case scenario, under voltage load shedding is implemented in the islanded DC microgrid. The different parameters of the NMG system are shown in Table 1.

5.1. Test Case 1: Islanding of DC Microgrid. Initially, the NMG system operates in grid-connected mode, where all microgrids are grid-connected and interconnected. In the grid-connected mode of each microgrid, the DG unit and the distribution grid in that microgrid meet the load's real and reactive power demand. Each distribution grid regulates the voltage of its respective microgrid in this mode. Also, power flows in the interconnecting lines are maintained at 0 MW and 0 MVAr and each distribution grid is made to supply 1 MW to the load in the respective microgrid. According to the explanation in Section 4, the NMG controller sends the desired reference signals for real and reactive powers to the LCs of the DG inverters and converters during grid-connected and islanded conditions. The DG inverter in each AC microgrid supplies 1 MW and 1 MVAr to the respective load. During the AC microgrid's grid-connected-mode, the AC microgrid's battery inverter acts as a back-up and does not supply real and reactive powers. In grid-connected mode of the DC microgrid, the DG converter supplies 1 MW to the load, whereas converters of battery and supercapacitor units do not supply any real power initially. So, in this way, during the steady-state grid-connected operation, load demand is satisfied in each microgrid in the NMG system. For $0 \le t < 1$ s, DC microgrid 2 is simulated in grid-connected mode, and the system's corresponding real and reactive power flows are shown in Figure 9.

For study purpose, the islanding of the DC microgrid is simulated. The real and reactive power flows during the islanded operation are shown in Figure 10. At $t = 1$ s, a three-phase balanced fault occurs at point "G" (shown in Figure 1) near distribution grid 2. This fault causes distribution grid 2 voltage to sag severely from 230 V (rms) to 11.5 V (rms) for $1 \le t < 1.2$ s as shown in Figure 11. Consequently, the interfacing AC/DC converter connected to distribution grid 2 cannot control DC load 2 bus voltage and the power supplied by distribution grid 2 reduces to almost 0 W. A power shortage in a DC microgrid causes DC load bus voltage to drop [28]. Thus, at the instant of fault, DC load 2 bus voltage drops from its nominal value of 380 V to 373 V at $t = 1$ s as shown in Figure 12. But the supercapacitor converter 2c operating in CCM is tasked by its local controller and the NMG controller to quickly supply a power output of 1 MW for a very short duration of 0.2 s for $1 \le t \le 1.2$ s as shown in Figure 13 until the battery converter 2b operating in VCM ramps up its power output from 0 MW to 1 MW for $1 \le t \le 1.2$ s as observed in Figure 14. Therefore, as shown in Figure 12, DC load 2 bus voltage gets restored temporarily to its nominal value of 380 V for $t > 1.05$ s. But at $t = 1.2$ s, the circuit breaker in the line interconnecting AC/DC converter and distribution grid 2 is opened to clear the fault. As a result, DC load 2 bus voltage further drops to 370 V at $t = 1.2$ s. After opening the circuit breaker, DC microgrid 2 gets islanded from distribution grid 2. As battery converter 2b delivers a steady-state power of 1 MW for $t \ge 1.2$ s onwards, DC load 2 bus voltage is quickly restored to 380 V for $t > 1.25$ s as observed in Figure 12. All the real and reactive

Table 1: Parameters of the NMG system.

Parameter	Value
Inverter input voltage	$V_{dc2} = 800$ V
Loss resistance of inverter	$R = 1\,\mu\Omega$
LC filter of inverter	$L_f = 1\,\mu$H, $C_f = 0.02$ F
DC/DC converter input voltage	$V_{in} = 600$ V
DC/DC converter inductor	$L_m = 50\,\mu$H
DC/DC converter capacitor	$C_m = 600\,\mu$F
Supply voltage of distribution grid	$V_g = 22000/\sqrt{3}$ Vrms (phase)
Line resistance and inductance	$R_{ti} = 1.6\,\Omega$, $L_{ti} = 6$ mH ($i = 1, 2, 3$)
Leakage inductance of line transformers	$L_T = 21\,\mu$H
Details of different component ratings	
(a) DG units 1, 2, and 3	1 MW (max)
(b) Storage battery units 1, 2, and 3	1.1 MW (max), 1.1 MWh (max)
(c) Supercapacitor unit 2	2 MW (max), 1.1 kWh (max)
(d) Transformers	1.5 MVA, 22/0.4 kV
(e) AC loads 1 and 3	2 MW, 1 MVAr
(f) DC load 2	2 MW

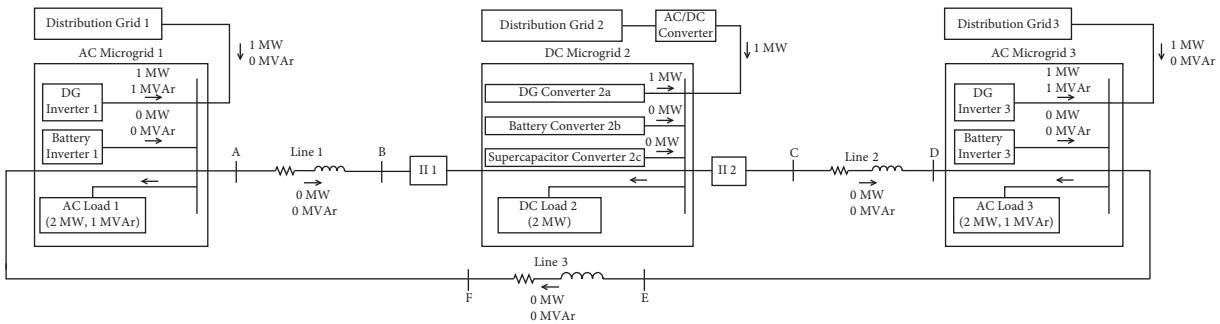

Figure 9: Real and reactive power flows and outputs in the NMG system during grid-connected operation.

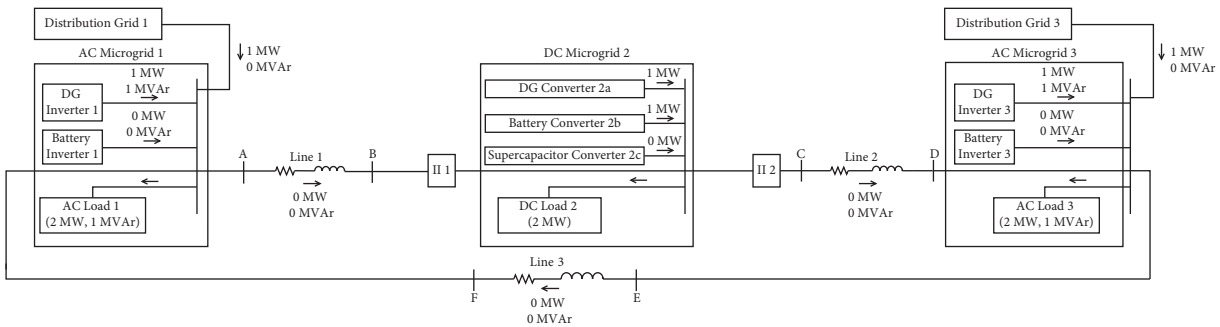

Figure 10: Real and reactive power flows and outputs in the NMG system when DC microgrid 2 gets islanded.

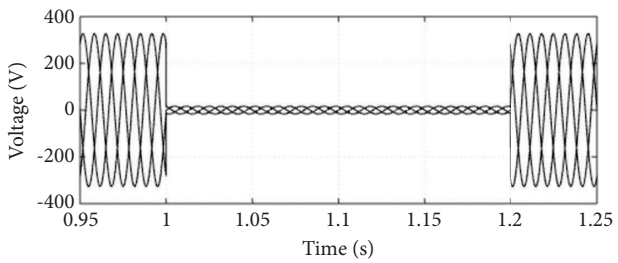

Figure 11: AC voltage at point "*G*" on the distribution grid 2 side.

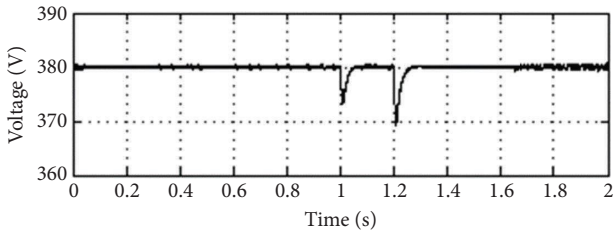

Figure 12: DC load 2 bus voltage.

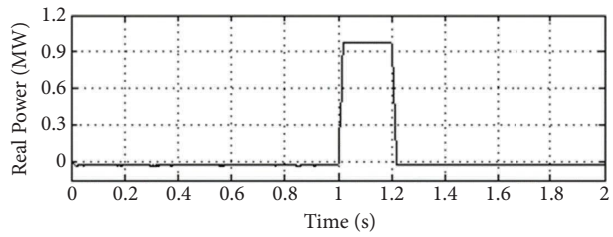

Figure 13: Real power output of supercapacitor converter 2c.

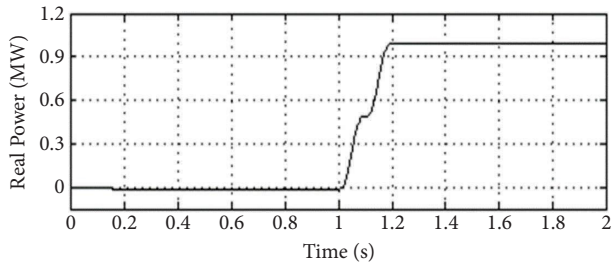

Figure 14: Real power output of battery converter 2b.

power flows in the NMG system during islanding of DC microgrid 2 are shown in Figure 10. From Figures 13 and 14, it can be observed that local MPC controllers for the converters are quickly able to track the reference power signals.

In conclusion, in this test case, the coordinated control of the supercapacitor and battery converters in the NMG system is achieved with the proposed control system's help and the desired DC load bus voltage and power flows are attained.

5.2. Test Case 2: Power Exchange between DC and AC Microgrids. The benefit of mutual power sharing among the microgrids in the second test case is highlighted. At $t = 3$ s, an increase of DC load from 2 MW to 4 MW is simulated in islanded DC microgrid 2, which can be inferred by comparing Figures 10 and 15. The DG and battery units in DC microgrid 2 are already operating at their maximum powers. The supercapacitor unit in DC microgrid 2 can give a real power output of 2 MW but for only a very short duration. Thus, DC microgrid 2 will not be able to meet the increase in its local load demand, and as a result, DC load 2 bus voltage will dip. To restore the real power balance and mitigate this voltage dip, DC microgrid 2 takes 1 MW each from microgrids 1 and 3 following the contract agreement among the microgrids, as shown in Figure 15. The proposed control system facilitates this power exchange explained in Section 4.

To transfer the required power from microgrids 1 and 3 to microgrid 2, the reference phase angles of the output voltages of the interconnecting inverters 1 and 2 need to be maintained equal to the value calculated from (25). The centralized controller then sends this voltage reference $230\angle -0.5^{\circ}$ V to the LCs of the interconnecting inverters. As observed in Figure 16, to avoid any voltage instability, the magnitude of the output voltage of the interconnecting inverters is always maintained at 230 V (rms phase-to-neutral). To facilitate the power transfer, the phase angles of the output voltages of the interconnecting inverters are thus maintained at -0.5° for $t > 3$ s as shown in Figure 17. As soon as the phase angles of these output voltages are changed from 0° to -0.5°, the real and reactive power flows through lines 1 and 2 are increased according to (1)–(4). Therefore, in lines 1 and 2, the desired sending and receiving end real powers equal to 1.01 MW and 1 MW, respectively, are obtained as shown in Figure 18. Then, as per (3) and (4) and as shown in Figure 19, the corresponding reactive powers thus obtained in both the lines at the sending and receiving ends are equal to 0.84 MVAr and 0.85 MVAr, respectively.

To meet the load demand in islanded DC microgrid 2, supercapacitor converter 2c and battery inverters 1 and 3 are tasked by the centralized controller and corresponding local controllers to supply the required real powers. As battery inverters 1 and 3 need approximately 0.2 s to ramp up their power outputs, supercapacitor converter 2c operating in CCM supplies real power output of 2 MW for 0.2 s from $t = 3$ s to $t = 3.2$ s as observed in Figure 20. To achieve the required real power flow in lines 1 and 2, the real power outputs of battery inverters 1 and 3 are controlled to increase from 0 MW to 1.01 MW for $t > 3$ s as shown in Figure 21. For $t > 3$ s, the real power output of battery converter 2b is maintained here same as before in test case 1, at 1 MW itself. The interconnecting inverters are made to supply the required receiving end reactive powers in lines 1 and 2. In order to achieve reactive power balance in AC microgrids 1 and 3, the reactive power outputs of DG inverters 1 and 3 are here reduced by the proposed control system from their previous values of 1 MVAr to 0.16 MVAr presently, as shown in Figure 15. Also, as shown in Figure 15, the magnitude and direction of all the real and reactive power flows and exchanges in the NMG system are represented for this test case. Moreover, as observed in test cases 1 and 2, MPC controllers for all the converters and inverters need only a period of about 10 cycles to quickly track and settle to the real power reference signals.

During load variation in islanded DC microgrid 2, the resulting power imbalance in DC microgrid 2 causes DC load 2 bus voltage to drop from the nominal value of 380 V to 363 V at $t = 3$ s as observed in Figure 22. On detection of this voltage drop by the centralized controller, the supercapacitor converter, battery inverters, and converter are tasked to supply the required real power at $t = 3$ s, as previously mentioned, to satisfy the load demand in DC microgrid 2 and to restore DC load 2 bus voltage. Thus, for $t > 3.08$ s, DC load 2 bus voltage is restored to its nominal value of 380 V, and voltage stability can thus be ensured in the islanded DC microgrid in the proposed NMG system.

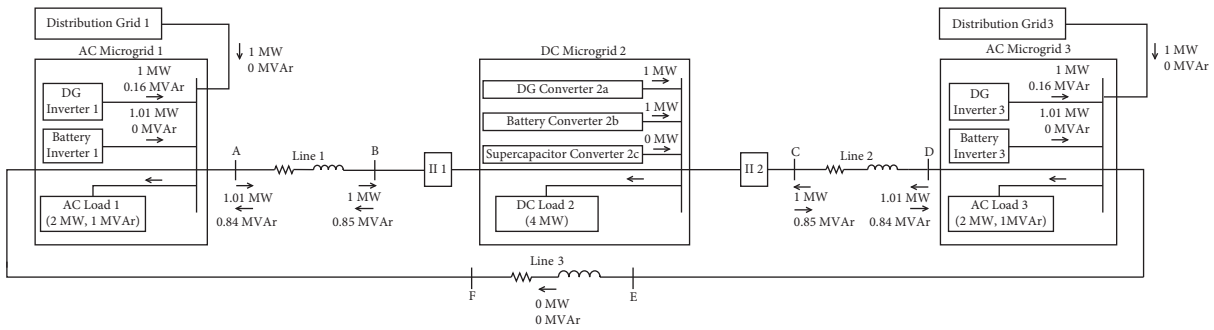

Figure 15: Real and reactive power exchange in the NMG system during load variation in DC MG 2.

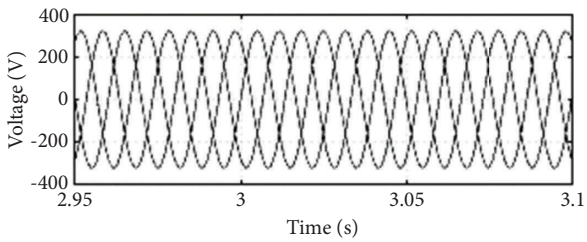

Figure 16: Three-phase output voltage of interconnecting inverters 1 and 2.

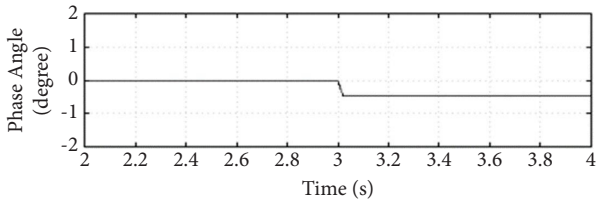

Figure 17: Phase angle of the output voltage of each of the interconnecting inverters.

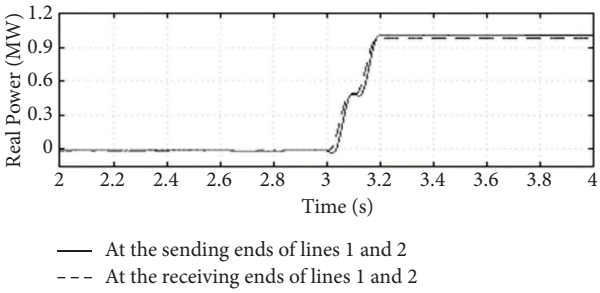

Figure 18: Magnitude of real powers at either ends of lines 1 and 2.

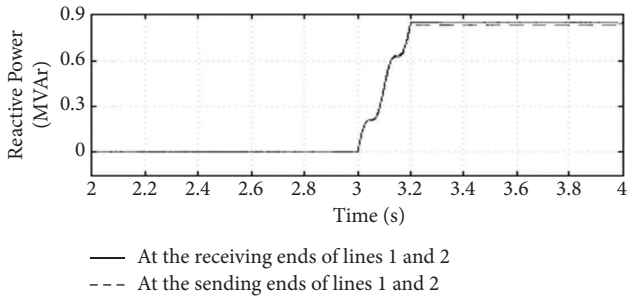

Figure 19: Magnitude of reactive powers at either ends of lines 1 and 2.

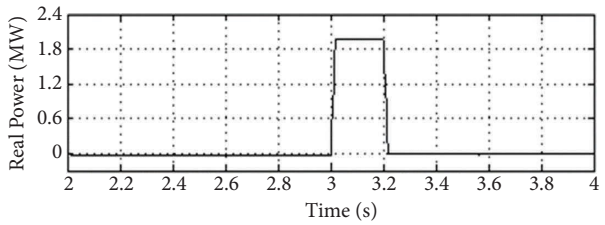

Figure 20: Real power output of supercapacitor converter 2c.

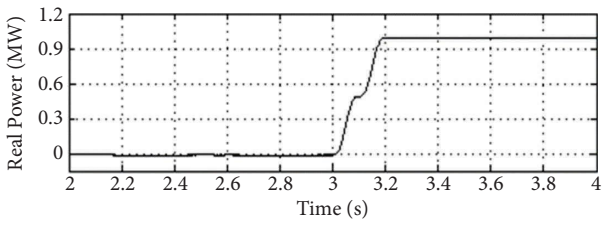

Figure 21: Magnitude of real power outputs of battery inverters 1 and 3.

5.3. Test Case 3: Under Voltage Load Shedding (UVLS) in Islanded DC Microgrid. This test case shows the implementation of UVLS under the power-deficit condition in the islanded DC microgrid shown in test case 2. At $t = 8$ s, DG converter 2a fails to operate. It is thus disconnected, as observed in Figure 23. Due to the disconnection of DG converter 2a, there is a shortage of real power of 1 MW in islanded DC microgrid 2 in the NMG system, which can be inferred from Figure 15. In the given islanded microgrid, all the battery inverters and converters are operating already at their maximum powers. As a result, at $t = 8$ s, supercapacitor converter 2c is tasked by the centralized controller to deliver the required power of 1 MW at rated energy for a fixed discharge time duration of supercapacitor unit 2, which is 4 s (i.e., in this case, maximum discharge time duration of supercapacitor unit 2 = rated energy of supercapacitor unit 2/power delivered by supercapacitor unit $2 = 0.0011$ MWh/1 MW $= 0.0011\,h = 4$ s). Therefore, supercapacitor converter 2c delivers 1 MW for $8 \le t \le 12$ s, as shown in Figure 24.

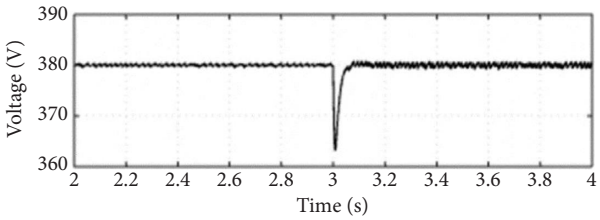

Figure 22: DC load 2 bus voltage.

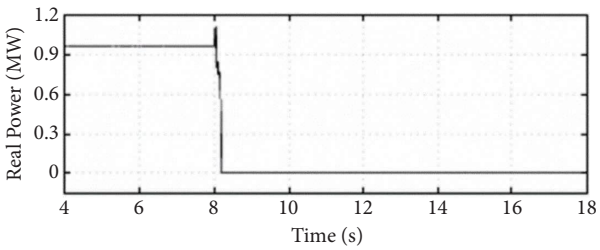

Figure 23: Real power output of DG converter 2a.

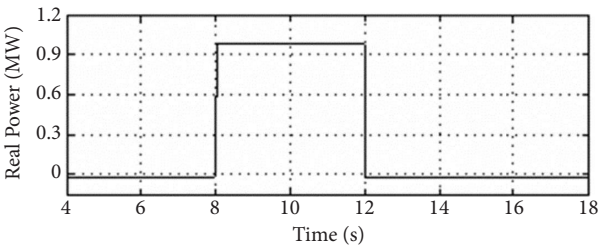

Figure 24: Real power output of supercapacitor converter 2c.

During the disconnection of DG converter 2a, DC load 2 bus voltage drops to 374 V at $t = 8.3$ s, as observed in Figure 25. Due to the supply of the required power by the supercapacitor converter 2c, DC load 2 bus voltage now gets restored back to 380 V for $t > 9$ s and is maintained at 380 V for $9 \le t \le 12$ s. For $t > 12$ s, when supercapacitor unit 2 gets discharged completely, a power deficit again occurs in DC microgrid 2, which causes DC load 2 bus voltage to drop to a very low value beyond the tolerance limit of ±19 V, as shown in Figure 25. The zoomed-in view of DC load 2 bus voltage for $12 \le t \le 12.9$ s is shown in Figure 26.

For restoring DC load 2 bus voltage, under voltage load shedding, as explained in Section 4, is implemented by the centralized controller as follows: (1) when DC load 2 bus voltage drops to 361 V at $t = 12.1$ s as shown in Figure 26, 15% of total load (i.e., 15% of 4 MW = 0.6 MW) is shed in DC microgrid 2 as observed in Figure 27; and (2) when DC load 2 bus voltage drops to 354 V at $t = 12.2$ s as seen in Figure 26, 10% of total load (i.e., 10% of 4 MW = 0.4 MW) is shed in DC microgrid 2 as shown in Figure 27. Due to this load-shedding scheme, DC load 2 bus voltage is restored to its nominal value of 380 V for $t \ge 13.5$ s as observed in Figure 25.

Like the load shedding scheme adopted in [29], different load shedding stages are also initiated within a very short delay of 0.1 s here. Moreover, the magnitude and

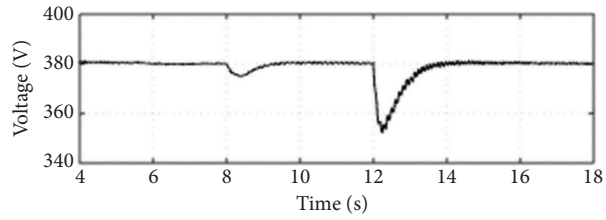

Figure 25: DC load 2 bus voltage.

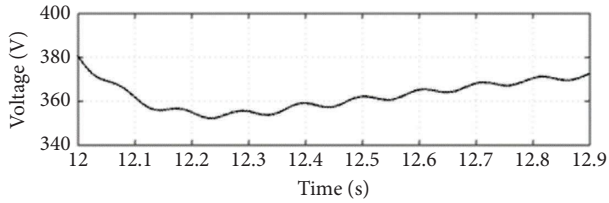

Figure 26: Zoomed-in view of DC load 2 bus voltage for $12 \le t \le 12.9$ s.

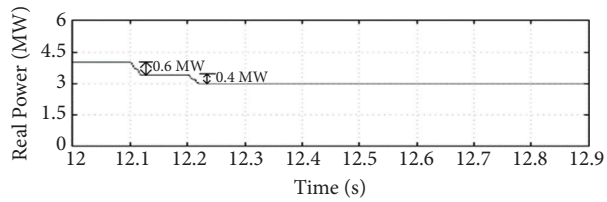

Figure 27: Magnitude of real power consumption of load 2 for $12 \le t \le 12.9$ s.

duration of the DC voltage dip in this test case are within the allowable tolerance limits to avoid the maloperation of DC load 2, as per the new DC version of the CBEMA (Computer and Business Equipment Manufacturers Association) curve [30].

6. Comparison between MPC and PI Controllers

In this section, the performance of two controllers, namely, the proposed MPC controller and the conventional PI controller, is compared similarly to [31]. The real power output of battery inverter 1 in the NMG system is controlled by MPC and PI methods and then compared. The PI controller applied here uses voltage and current control loops to regulate the real power output of battery inverter 1. The theory behind the PI controllers is discussed in [32].

As shown in Figure 28, the real power output of battery inverter 1 is maintained at 0 MW for $0 > t > 4$ s and at 1 MW for $4 > t > 12$ s using PI and MPC controllers. From this figure, the tracking error and delay time for set-point change are calculated for both the controllers and listed in Table 2.

From Table 2, it can be inferred that MPC exhibits better performance in terms of lower tracking error and faster set-point change. Specifically, the tracking error of MPC is 50% lower than that of PI control, and the delay time for a set-point change in the case of MPC is 33.33% lower than that of PI control.

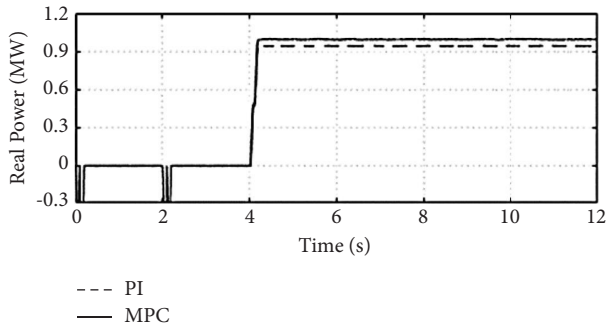

Figure 28: Real power output of battery inverter 1.

Table 2: Performance parameters of MPC and PI controllers [31].

Parameters	PI	MPC
Tracking error (%)	0.8	0.4
Delay time for set-point change	15 cycles (0.3 s)	10 cycles (0.2 s)

7. Conclusion

A control system is presented in this paper for a ring-shaped NMG system to rectify the problems of DC voltage variation and power imbalance during instances of islanding and load changes. Also, an advanced MPC algorithm has been proposed to control multiple DC/DC and DC/AC converters in the proposed NMG system. Various simulation studies are carried out to verify the functioning of the developed control system. The simulation results show that the proposed control system achieves satisfactory performance and regulates the power exchanges among microgrids during different operating conditions of the NMG system. Moreover, the proposed MPC algorithm is compared with a conventional PI algorithm, and it is found that MPC achieves a reduced tracking error, which is 50% lower than that of PI. Therefore, an efficiently managed control system and algorithm maintain the desired voltage stability and power exchange capability in the NMG system. The developed NMG architecture presented in this paper can be the first step towards hardware-in-the-loop testing and implementation.

Data Availability

The data used to support the findings of this study are available from the corresponding author upon reasonable request.

Disclosure

The contents presented in this paper are available in Chapter 4 in the doctoral thesis [22] written and published by the first author.

Conflicts of Interest

The authors declare that there are no conflicts of interest regarding the publication of this paper.

Acknowledgments

The first author would like to thank Nanyang Technological University, Singapore, for granting him doctoral research scholarship. Open-access funding was enabled and organized by JISC.

References

[1] N. Hatziargyriou, *Microgrids: Architectures and Control*, Wiley, Chichester, UK, 2014.

[2] M. N. Alam, S. Chakrabarti, and A. Ghosh, "Networked microgrids: state-of-the-art and future perspectives," *IEEE Transactions on Industrial Informatics*, vol. 15, no. 3, pp. 1238–1250, 2019.

[3] M. Shahidepour, Z. Li, S. Bahramirad, Z. Li, and W. Tian, "Networked microgrids," *IEEE Power and Energy Magazine*, vol. 17, pp. 63–71, 2017.

[4] B. Zhao, X. Zhang, and J. Chen, "Integrated microgrid laboratory system," *IEEE Transactions on Power Systems*, vol. 27, no. 4, pp. 2175–2185, 2012.

[5] G. Turner, J. P. Kelley, C. L. Storm, D. A. Wetz, and W. Lee, "Design and active control of a microgrid test bed," *IEEE Transactions on Smart Grid*, vol. 6, no. 1, pp. 73–81, 2015.

[6] I. U. Nutkani, P. Loh, and F. Blaabjerg, "Distributed operation of interlinked AC microgrids with dynamic active and reactive power tuning," *IEEE Transactions on Industry Applications*, vol. 49, no. 5, pp. 2188–2196, 2013.

[7] S. Moayedi and A. Davoudi, "Distributed tertiary control of DC microgrid clusters," *IEEE Transactions on Power Electronics*, vol. 31, no. 2, pp. 1717–1733, 2016.

[8] X. Liu, P. Wang, and P. C. Loh, "A hybrid AC/DC microgrid and its coordination control," *IEEE Transactions on Smart Grid*, vol. 2, no. 2, pp. 278–286, 2011.

[9] L. Che, M. Shahidehpour, A. Alabdulwahab, and Y. Al-Turki, "Hierarchical coordination of a community microgrid with AC and DC microgrids," *IEEE Transactions on Smart Grid*, vol. 6, no. 6, pp. 3042–3051, 2015.

[10] H. Zhang, J. Zhou, Q. Sun, J. M. Guerrero, and D. Ma, "Data driven control for interlinked AC/DC microgrids via model-free adaptive control and dual droop control," *IEEE Transactions on Smart Grid*, vol. 23, no. 99, pp. 1–15, 2015.

[11] N. Eghtedarpour and E. Farjah, "Power control and management in a hybrid AC/DC microgrid," *IEEE Transactions on Smart Grid*, vol. 5, no. 3, pp. 1494–1505, 2014.

[12] M. Islam, F. Yang, and M. Amin, "Control and optimisation of networked microgrids: a review," *IET Renewable Power Generation*, vol. 15, no. 6, pp. 1133–1148, 2021.

[13] C. Guzman, A. Cardenas, and K. Agbossou, "Load sharing strategy for autonomous AC microgrids based on FPGA implementation of adaline & fll," *IEEE Transactions on Energy Conversion*, vol. 29, no. 3, pp. 663–672, 2014.

[14] V. Nasirian, A. Davoudi, F. L. Lewis, and J. M. Guerrero, "Distributed adaptive droop control for DC distribution systems," *IEEE Transactions on Energy Conversion*, vol. 29, no. 4, pp. 944–956, 2014.

[15] S. M. Ashabani and Y. A. R. I. Mohamed, "General interface for power management of micro-grids using non-linear cooperative droop control," *IEEE Transactions on Power Systems*, vol. 28, no. 3, pp. 2929–2941, 2013.

[16] L. Y. Lu and C. C. Chu, "Consensus-based droop control synthesis for multiple DICs in isolated microgrids," *IEEE Transactions on Power Systems*, vol. 30, no. 5, pp. 2243–2256, 2015.

[17] J. Rodriguez and P. Cortes, *Predictive Control of Power Converters and Electrical Drives*, Wiley, Chichester, UK, 2012.

[18] K. S. Low and R. Cao, "Model predictive control of parallel connected inverters for uninterruptible power supplies," *IEEE Transactions on Industrial Electronics*, vol. 55, no. 8, pp. 2884–2893, 2008.

[19] Z. Zhang, O. Babayomi, T. Dragicevic et al., "Advances and opportunities in the model predictive control of microgrids: part 1- primary layer," *International Journal of Electrical Power & Energy Systems*, vol. 134, 2022.

[20] O. Babayomi, Z. Zhang, T. Dragicevic et al., "Advances and opportunities in the model predictive control of microgrids: part- II secondary and tertiary layers," *International Journal of Electrical Power & Energy Systems*, vol. 134, Article ID 107339, 2022.

[21] F. Kamal and B. Chowdhury, "Model predictive control and optimization of networked microgrids," *International Journal of Electrical Power & Energy Systems*, vol. 138, Article ID 107804, 2022.

[22] bitstream, "Operation and control of multi-area multi-microgrid systems," 2020, https://dr.ntu.edu.sg/bitstream/10356/72682/1/Final_Hardbound_PhD%20Thesis_John%20Thomas_G1200.

[23] P. Kundur, *Power System Stability and Control*, McGraw-Hill, New York, NY, USA, 1994.

[24] L. Wang, *Model Predictive Control System Design and Implementation Using MATLAB*, Springer, London, UK, 2009.

[25] D. E. Olivares, A. Mehrizi-Sani, A. H. Etemadi et al., "Trends in microgrid control," *IEEE Transactions on Smart Grid*, vol. 5, no. 4, pp. 1905–1919, 2014.

[26] J. Xiao, L. Setyawan, P. Wang, and C. Jin, "Power capacity-based bus-voltage region partition and online droop coefficient tuning for real-time operation of DC microgrids," *IEEE Transactions on Energy Conversion*, vol. 30, no. 4, pp. 1338–1347, 2015.

[27] Reliability, "Under voltage load sheding guidelines," 2023, https://beckwithelectric.com/wp-content/uploads/docs/tech-docs/Protective-Relays/Beckwith-Undervoltage-Load-Shedding.pdf.

[28] D. Chen, L. Xu, and L. Yao, "DC voltage variation based autonomous control of DC microgrids," *IEEE Transactions on Power Delivery*, vol. 28, no. 2, pp. 637–648, 2013.

[29] P. M. Anderson and M. Mirheydar, "An adaptive method for setting underfrequency load shedding relays," *IEEE Transactions on Power Systems*, vol. 7, no. 2, pp. 647–655, 1992.

[30] portal, "Residential and commercial use of DC power," 2020, http://portal.emergealliance.org/DesktopModules/Inventure_Document/FileDownload.aspx?ContentID=20144.

[31] T. John, C. Patsios, and D. Greenwood, "Non-local harmonic current and reactive power compensation for a multi-microgrid system using a series-shunt network device," *IET Generation, Transmission & Distribution*, vol. 14, no. 23, pp. 5655–5666, 2020.

[32] J. Lopes, C. L. Moreira, and A. Madureira, "Defining control strategies for microgrids islanded operation," *IEEE Transactions on Power Systems*, vol. 21, no. 2, pp. 916–924, 2006.